Modern Applied Science; Vol. 8, No. 4; 2014
ISSN 1913-1844 E-ISSN 1913-1852
Published by Canadian Center of Science and Education

Piezoelectric Energy Harvesting from Wind Using Coupled Bending-Torsional Vibrations

Arvind Deivasigamani[1], Jesse M. McCarthy[1], Sabu John[1], Simon Watkins[1], Pavel Trivailo[1] & Floreana Coman[2]

[1] School of Aerospace, Mechanical and Manufacturing Engineering, RMIT University, Bundoora, Victoria, Australia

[2] FCST Pty. Ltd., Melbourne, Australia

Correspondence: Arvind Deivasigamani, Post-Graduate Research student, School of Aerospace, Mechanical and Manufacturing Engineering, RMIT University, PO Box 71, Bundoora, Victoria, 3083, Australia. Tel: 61-425-564-825. E-mail: arvind1288@gmail.com

Received: April 24, 2014 Accepted: May 23, 2014 Online Published: June 25, 2014

doi:10.5539/mas.v8n4p106 URL: http://dx.doi.org/10.5539/mas.v8n4p106

Abstract

Energy harvesting using Polyvinylidene-fluoride (PVDF) piezoelectric beams from fluid-induced flutter was studied. Vibration tests were performed to compare the power output of a piezoelectric beam subject to bending, and coupled bending-torsion loading conditions. A piezoelectric, harmonic computational analysis was done to further investigate the effect of the bending-torsion loading condition. It was evident that by inciting bending and torsion in the beam simultaneously, higher power outputs were achieved. However, when the tests were conducted in a wind tunnel with fluid forcing as opposed to steady-state vibration, the power output of the combined bending and torsion case was much lower than the bending-only case. High-speed image data indicated that the configurations subjected to bending-torsion flutter had lower bending deformations and were more prone to chaotic flapping, which inherently resulted in reduced power outputs. Finally, a vertical stalk configuration was examined, which produced five times more power compared to the horizontal stalk configuration at 8m/s wind speed due to excessive non-linear bending.

Keywords: fluid-induced flutter, piezoelectric energy harvesting, bending-torsional vibrations, dual field computational analysis

1. Introduction

Energy harvesting has been, and will continue to be, an important area for researchers. Piezoelectric materials have played an important role, since they can transduce mechanical vibrations into electrical energy. Recently, flutter has been exploited to generate electrical energy from compliant piezoelectric materials, such as PVDF. This concept was initially studied only with an academic interest but was later used for practical engineering purposes (Païdoussis, 1998). There has been extensive work done elsewhere to understand flutter of plates and membranes (Lord Rayleigh, 1879; Theodorsen, 1949; Datta and Gottenberg, 1975; Argentina and Mahadevan, 2005).

In 2001, the concept of an energy harvesting 'eel' was introduced (Allen and Smits, 2001). The 'eel' consisted of a PVDF-laden membrane clamped at its leading edge. The eel was placed in a parallel flow, downstream of a vortex shedding bluff body that induced time-varying deformations of the eel, according to the vortex shedding frequency.

Scaling up an energy harvester system using a matrix-like array of piezoelectric patches immersed in water was proposed in Pobering and Schwesinger (2004). It was suggested that this scaled-up piezoelectric energy harvesting system generated more power per unit volume than a small wind turbine; however, this was based solely on a theoretical approximation. Elsewhere, an artificial tree comprising of piezoelectric “stalks” and polymeric “leaves” was conceptualized in Dickson, 2008. There, the leaves of the tree were coupled via a revolute hinge to the piezoelectric stalks. The idea was that as wind swept across the tree, flutter of the leaf-stalks would result and electrical power would be generated and subsequently stored. The motivation behind this design was to have a safe, aesthetically pleasing device that could power Ultra Low Power (ULP) devices such as sensors and LED lights.

The artificial tree concept was tested with a single PVDF-leaf configuration in parallel smooth flow (Li & Lipson, 2009). Two different configurations, namely a horizontal stalk and vertical stalk, were tested (Figure 1).

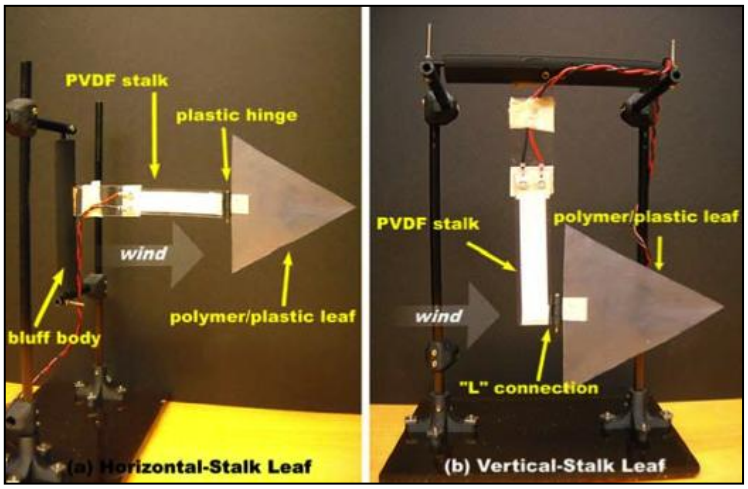

Figure 1. Horizontal and vertical leaf stalk configuration (Li and Lipson, 2009)

It was found that the vertical-stalk arrangement output higher power compared to the horizontal stalk arrangement. However, the reasons for the increased power output were not known. It was hypothesized that the vertical-stalk configuration was subjected to coupled bending-torsion vibration modes, leading to more power output. In Bryant et al. (2011), a similar horizontal-stalk energy harvesting device was investigated, which consisted of a Lead-Zirconate-Titanate (PZT) patch bonded to a compliant steel beam, which in turn was connected to a flutter amplifier via a hinge.

In Li et al. (2011), different leaf geometries were examined and it was shown that the triangular leaf caused the system to output the most power, though it was not known why. In McCarthy et al. (2012), different triangular-leaf aspect ratios and areas were studied and it was found that an isosceles triangle with base and height, each 8cm, was the optimum shape and size in terms of power output. In Deivasigamani et al. (2013), a parametric study was carried out, which involved varying the hinge placement at different span-wise locations along a highly compliant beam immersed in a parallel flow. The effect of different hinge positions on the flutter characteristics of the beam was studied and it was shown that by simply altering the hinge location, the flutter frequency, mode-shape, and flutter cut-in speed could be varied appreciably.

In the case of a symmetrical beam in a parallel flow, flutter most often manifests in a bending mode of the beam, and very little torsion occurs. Abdelkefil et al. (2011) investigated a piezoelectric cantilever beam subjected to coupled bending–torsional vibrations via base excitation, due to an imposed offset between the beam centre of mass and shear centre. The offset was created by placing two masses asymmetrically at the tip of the beam (Figure 2). It was shown analytically that a piezoelectric beam subjected to coupled bending-torsion output nearly 30% more power than a beam subjected to conventional transverse bending. However, no experiments were performed to validate their results.

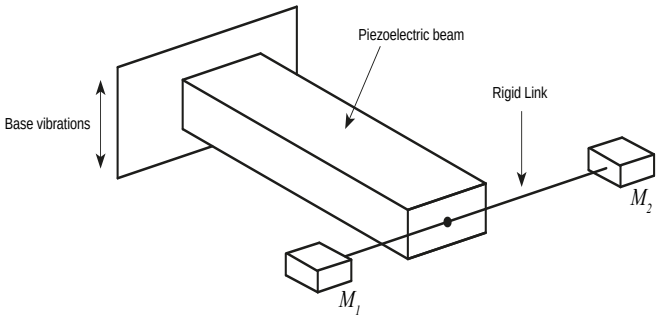

Figure 2. Schematic diagram of asymmetrical energy harvesting system (Abdelkefil et al., 2011)

In the work presented here, the experiments performed by Li and Lipson (2009) and Abdelkefil et al. (2011) were combined to investigate the performance of an asymmetric piezoelectric leaf-stalk system immersed in a parallel flow. Thus, the main objectives are

- To perform simple dynamic tests utilizing a shaker with the PVDF configurations to identify the effect of coupled bending-torsion vibrations on the power output.
- To perform dual field computational analysis with the symmetrical and asymmetrical configurations to validate the experimental results.
- To carry out wind-tunnel tests in smooth flow with the symmetrical, asymmetrical and vertical PVDF-hinge-leaf configurations and compare the power outputs.
- To identify the flutter modes and behavior of the configurations using high-speed camera footages.

2. Theoretical Concept of Coupled Bending-Torsional Vibrations

Whenever a beam experiences transverse loading away from its centroidal axis, it is subjected to coupled bending and torsion. This means that instead of a single bending equation, the motion is actually governed by a system of two equations that need to be solved simultaneously. The equations are given by Weaver et al. (1990) as:

$$m\frac{\partial^2\left(y-b\theta\right)}{\partial t^2}+YI\frac{\partial^4 y}{\partial x^4}=f(t) \tag{1}$$

$$mc\frac{\partial^2\left(y-b\theta\right)}{\partial t^2}+R\frac{\partial^2\theta}{\partial x^2}-R_1\frac{\partial^4\theta}{\partial x^4}-\rho_s I_p\frac{\partial^2\theta}{\partial t^2}=f(t) \tag{2}$$

where $m = \rho_s hl$, the mass per unit length of the beam; ρ_s - density of the beam; h - thickness of the beam; l- width of the beam; Y- Young's modulus; I- moment of inertia; $f(t)$ - transverse loading function; b - distance between the centroidal axis of the beam and its shear center; I_p - polar moment of inertia; R - torsional rigidity and R_1 - warping rigidity.

The stress (T) and the strain (S) induced from coupled bending-torsion are then:

$$T=\frac{Mz}{I}=-z\left(Y\frac{\partial^2 y}{\partial x^2}+G\frac{\partial^2\theta}{\partial x^2}\right) \tag{3}$$

$$S=-z\left(\frac{\partial^2 y}{\partial x^2}+\frac{\partial^2\theta}{\partial x^2}\right) \tag{4}$$

where G - shear modulus and z - distance from neutral axis to the point of interest. The stress and strain induced via the beam vibrations are related to the electric field and displacement by (Erturk & Inman, 2011):

$$\begin{bmatrix} S \\ D \end{bmatrix}=\begin{bmatrix} c & d \\ d^t & \varepsilon \end{bmatrix}\begin{bmatrix} T \\ E \end{bmatrix} \tag{5}$$

Where D – electrical displacement; c – compliance; d- direct piezoelectric coefficient; d_t – transverse piezoelectric coefficient, ε- permittivity; E - electric field strength.

It is non-trivial to obtain a closed-form solution for Equations (1), (2) and (5). Since piezoelectric energy harvesting involves conversion of mechanical energy to electrical energy, it could be sufficient to perform a theoretical analysis on the mechanical energy produced in transverse bending and compare it with the mechanical energy produced in coupled bending-torsion. This analysis could later be verified with the electrical power output obtained from the experimental and computational studies. However, there are certain drawbacks in doing so: firstly, all of the strain energy is not harvestable. Since the piezoelectric beam acts as a strain integrator over the piezoelectric area, the shear strains produced from torsion do not contribute to the overall

harvestable energy unless the piezoelectric membrane is designed to work in the d_{15} mode (which converts shear strains into electrical energy). Secondly, it is important to note that the static strain energy equations do not consider the vibration frequency and damping present in any dynamic system.

Therefore, it is important to perform experiments and simulations to identify the effect of coupled bending-torsion vibrations which are explained in the following sections. The effect of damping in the system is also investigated in the following section.

3. Dynamic Tests

3.1 Experimental Setup

Dynamic tests were performed using a PVDF patch (LDT2-028K/L, Measurement Specialties, Inc.). Three different configurations were tested; The first configuration consisted of the PVDF only (Figure 3a), with the base completely clamped and the free end attached to a shaker (LS 100 - Ling Electronics) to input known transverse displacements at a specific frequency. The second configuration consisted of the PVDF clamped at one end, with a Mylar strip bonded orthogonally at the PVDF free end (Figure 3b). The free end of the Mylar was then connected to the shaker. The purpose of the Mylar strip was to create an offset between the centroidal axis of the PVDF and the shaker location. The length of the Mylar strip from the centroidal axis of the PVDF to the shaker was 36mm (half of the overall length of the PVDF patch). The third configuration was similar to the second configuration except that the offset distance was 72mm. Mylar was used here due to its relatively high specific modulus.

The three cases tested are summarized in Table 1, and the properties of the PVDF patch and Mylar are given in Table 2. The shaker was configured to input a constant sinusoidal displacement amplitude of 13mm at a frequency of 15Hz for all three cases. Given that all the configurations were compliant and low mass, the assumption of a constant input displacement amplitude was valid. The orientation of the tests was such that no sagging of the beams due to gravity occurred; the scope of this work excluded a study on the influence of gravity in these systems.

In order to data-log the electrical power output, the PVDF patch was connected to a simple circuit. The power output of a piezoelectric material depends on the external load resistance across which the voltages are measured (Kong et al., 2010). The optimal load resistance, R_{Lopt}, for a piezoelectric material, which will permit maximum power output, is estimated as:

$$R_{L_{\text{opt}}} \approx \frac{1}{\omega C} \tag{6}$$

where ω - forced frequency of the piezoelectric material and C - internal capacitance of the piezoelectric material. The PVDF patch was connected to a load resistance of 5.6MΩ in parallel. Since the PVDF patch was eventually tested in fluid flow, this optimum load resistance value was obtained experimentally for the mean flow velocity. The interested reader can find these load matching details in McCarthy et al. (2013). The circuit was then connected across a differential probe (Elditest, GE8115) before linking to a DAQ board (National Instruments, BNC 2110). The use of a differential probe with a high internal impedance ensured that the AC voltage from the patch was measured across the load resistance, and also that the voltage was scaled down to meet the maximum allowable voltage requirements of the DAQ board. The circuit diagram is shown in Figure 4.

The AC voltages were recorded at a sampling rate of 1kHz, for a period of two minutes, to ensure good resolution. A LabView® program was user-written to calculate the RMS voltage at 0.1-second intervals, thereby having 1200 values of RMS voltages for the recorded time frame. The electrical power output was then calculated for each interval as:

$$P_i = \frac{V_{RMS}^2}{R} \tag{7}$$

where V_{RMS} - root-mean-square voltage from the leaf-stalk. The average power for the two-minute interval was calculated as:

$$P_{mean} = \frac{1}{n}\sum_{i=1}^{1200} P_i \tag{8}$$

Table 1. A summary of the configurations tested in the experiments

Configuration 1	PVDF beam subjected to bending.
Configuration 2	PVDF beam subjected to bending and torsion with the shaker offset at *a* (36mm) via Mylar.
Configuration 3	PVDF beam subjected to bending and torsion with the shaker offset at 2*a* (72mm) via Mylar.

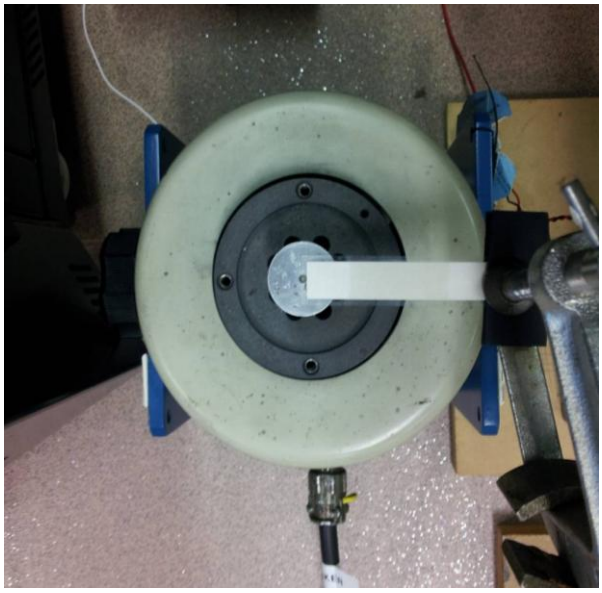

Figure 3a. Setup of bending configuration

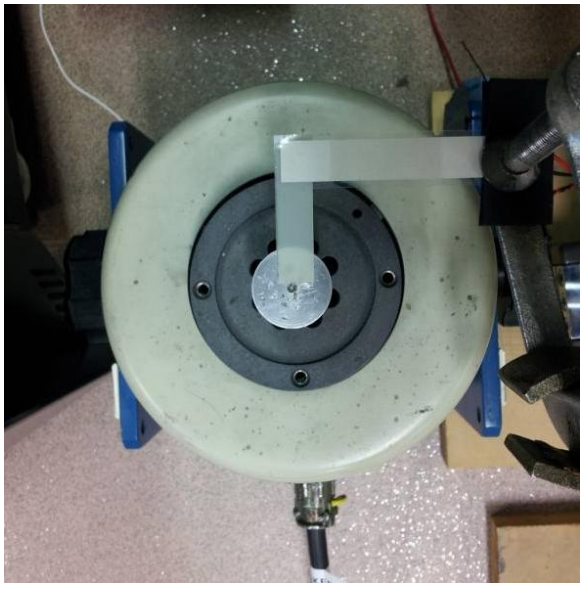

Figure 3b. Setup of asymmetric loading with offset distance of *a*

Table 2. Material properties

PVDF properties (LDT2-028K/L)	
Overall length (mm)	72
Width (mm)	16
Total Thickness (μm)	205
Young's Modulus (GPa)	3.0
Piezo stress coefficient, g_{31} (Vm/N)	0.216
Piezo stress coefficient, g_{32} (Vm/N)	0.003
Piezo stress coefficient, g_{33} (Vm/N)	-0.33
Density (kg/m^3)	1780
Poisson's ratio	0.34
Mylar properties	
Width (mm)	10
Thickness (mm)	0.35
Young's Modulus (GPa)	5.0
Density (kg/m^3)	1400

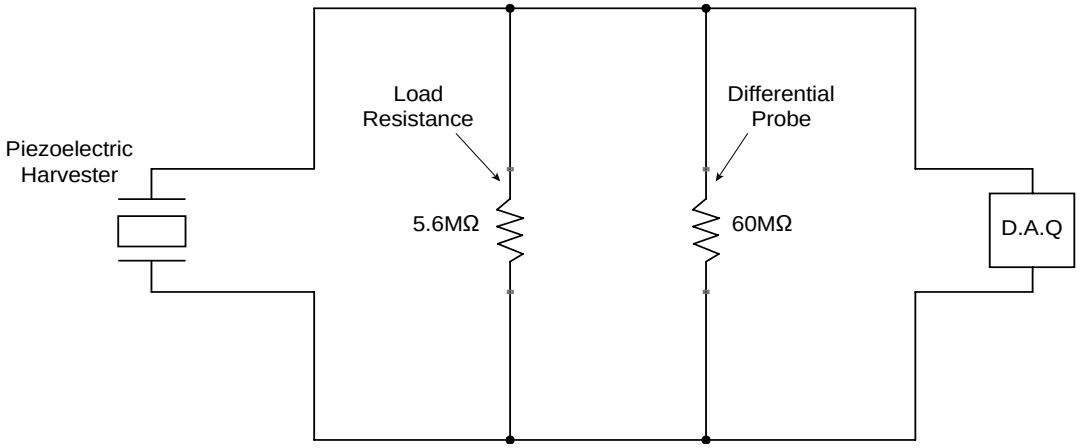

Figure 4. The parallel circuit used to measure power output from the energy harvester

3.2 Computational Modeling

3.2.1 Overview

In order to corroborate the experimental results from the shaker, a computational analysis was conducted utilising ANSYS® R14.0; specifically, the dual-field, piezoelectric capabilities of the code. Three different scenarios were investigated, matching the three cases outlined in Table 1; bending, bending and torsion with offset *a*, and bending and torsion with offset 2*a*. A steady-state harmonic analysis was carried out for each case, with the following assumptions made:

1. The material model was linearly elastic, and no material non-linear effects were taken into account.
2. Transient vibrational effects (i.e. start-up effects) were ignored.
3. The effect of gravity was ignored (as mentioned earlier).
4. No material viscoelastic or electrical damping was considered.

The geometry was modeled as per the experimental shaker setup, see Figure 5, with the PVDF patch clamped at one end and either free, as in the bending case, or bonded to the Mylar beam at the other end. A displacement boundary condition forcing the transverse displacement degree-of-freedom was implemented, so as to replicate the shaker's effect. All other degrees of freedom were fixed at the location of the imposed displacement. The forced displacement was applied as a sinusoidal input with an amplitude of 13mm and a frequency of 15Hz.

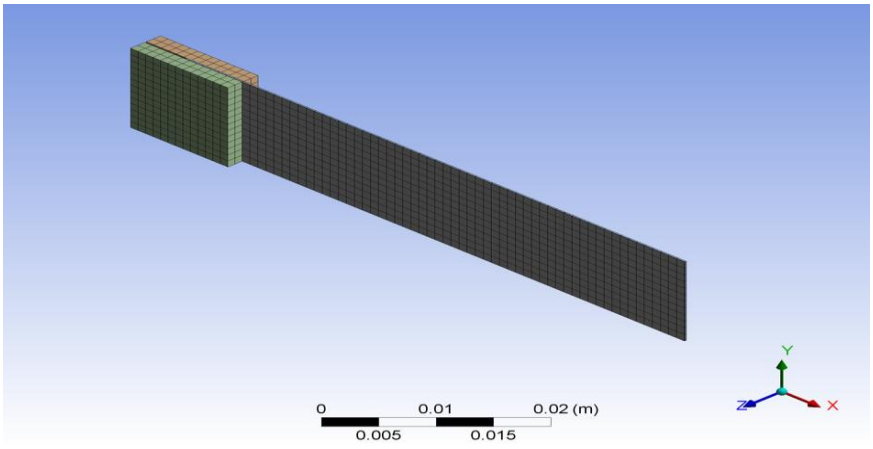

Figure 5a. Computational bending configuration

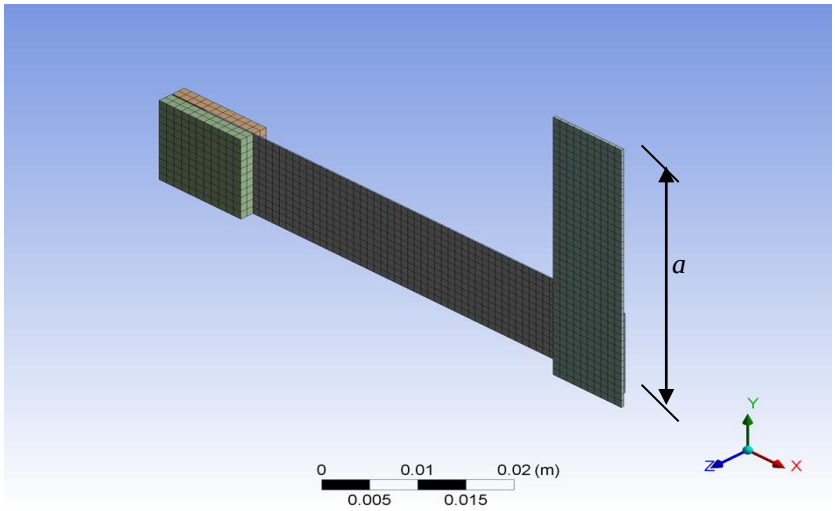

Figure 5b. Computational asymmetric loading case with offset distance *a*

The steady-state power output from the PVDF patch was measured by connecting a resistance element (with resistance 5.6MΩ) to the two terminals of the patch. A mesh sensitivity analysis revealed that large changes in the mesh sizing did not significantly affect the output power, and so a relatively fine mesh sizing was chosen, and kept constant across the three test cases (Figure 5) so as to isolate the effect of the increasing offset distance, and adequately capture the strains experienced during the loading. During the solution process, the equations of motion governing the harmonic response of the beam were solved directly, as iterative solvers caused poor performance with the dual-field elements meshed to the PVDF-beam geometry.

Instead of applying a clamped end condition to the PVDF beam, the actual clamps from the experiments were modeled in order to simulate the fact that a small section of the PVDF beam was clamped (Figure 5). The clamps were then fixed on all four edges to enforce the clamping end condition of the PVDF beam.

3.2.2 Structural Damping Analysis

The total amount of damping present in the experimental model would involve structural damping, fluid-added damping and electrical damping. Given the geometry of the structure, the fluid-added mass effects could be considered negligible. However, electrical damping could affect the dynamics of the system, especially when the load resistance is matched to the operating piezo (Sodano et al., 2001). Here, only the structural damping was taken into account, as:

$$\zeta_s = \frac{c}{c_{crit}} \tag{9}$$

where ζ_s is the global structural damping ratio, c is the user-defined structural damping applied, and c_{crit} is the structural critical damping coefficient, as calculated internally by the solver. The structural damping here is proportional to the strain induced in the structure, and is independent of the forcing frequency; whereas viscoelastic damping is proportional to the velocity of the structure, and can be shown to be linearly dependent on the forcing frequency (Beards, 1996). Here, we had ζs range from 0 to 1.4, and both the power output and torsional power ratio γ for each damping-ratio case was plotted. Here, a torsional power ratio, γ, is defined as:

$$\gamma = \frac{P_{2a} - P_{bending}}{P_a - P_{bending}} \tag{10}$$

where P_{2a} is the power output at *2a* offset, P_a is the power output at *a* offset, and $P_{bending}$ is the power output from bending only.

3.3 Results and Discussion

It is known from Priya (2007), that the harvestable energy from mechanical vibrations at resonance is given by:

$$P = \frac{mA^2\omega^3}{4\zeta^2} \tag{11}$$

where m - mass of the structure; A - amplitude of vibration; ω - frequency of vibration; ζ - damping ratio of the system. The general, off-resonance condition is likewise defined as (Priya, 2007):

$$P = \frac{\left(\frac{\omega}{\omega_i}\right)^4 mA^2\omega^3}{\left(1-\left(\frac{\omega}{\omega_i}\right)^2\right)^2 + \left(\frac{2\delta\omega}{\omega_i}\right)^2} \tag{12}$$

In the experimental analysis, an input displacement frequency of 15Hz was maintained for all three configurations and the power output recorded for two minutes. As seen in Equations (11) and (12), it was vital to maintain a constant frequency, as the input frequency would affect the power output, though the effect of changes in input frequency were not quantified in the analyses. Furthermore, damping is inversely proportional to power output. In the experiments, the structural damping ratio ζs for all the configurations was not measured and so in the computational analysis, it was varied from 0 to 1.4. Interestingly, for ζs = 0.7, the computational results corresponded almost exactly with the experimental results (Figure 6), indicating that the experiments could have indeed been in a 70% under-damped state.

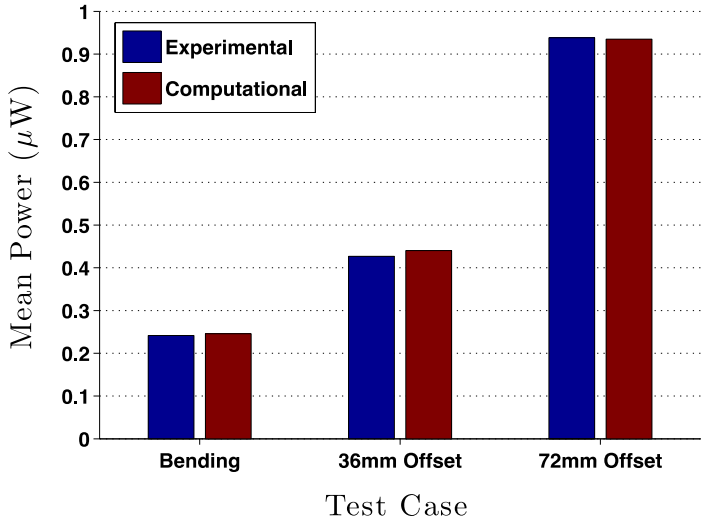

Figure 6. Comparison of experimental and computational shaker results

The offset configurations provided more power output compared to the bending case, as expected. The power outputs, in general, were low due to the relatively small applied displacements. The experimental power ratio was found to be 3.76 while the computational power ratio for ζs = 0.7 was 3.54. The computationally determined output power and power ratio for the three cases are compared against a varying damping ratio in Figure 7.

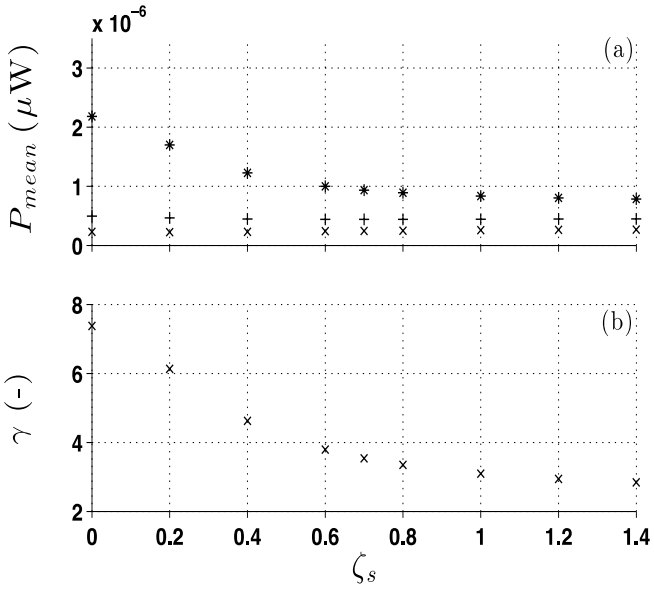

Figure 7. A plot showing the (a) computational power output and (b) power ratio against the structural damping ratio. For (a); x - bending, + - 36mm offset, * - 72mm offset

It was evident that the effect of the structural damping ratio was more pronounced for the *2a* offset case. This was probably due to the higher strains sustained in the Mylar due to inertia. Ideally, a material with infinite stiffness and zero mass would have been preferred to achieve the offset; but this cannot be practically achieved.

Ideally, the shaker tests must have been performed for a range of frequencies in order to get a proper result. Also, the damping ratio of the system must have been experimentally determined to be compared with the computational result. However, given the electrical and flexible nature of the PVDF, it is not trivial to eliminate electrical and viscoelastic damping effects in the experiments. Moreover, since the main focus of this paper is to identify the effect of bending and torsional vibrations on the power output during fluid-induced flutter, extensive shaker tests were not performed. Although the 0.7 damping ratio match was not very scientifically deduced, Figure 7 indicated the effect of damping on the increase in power output for all the three test cases. It indicated that for all the damping ratios, the power ratio was greater than 2, indicating that the coupled bending-torsion configurations provided higher power output at all cases. It was however important to investigate if these offset configurations performed similarly when excited by fluid flow. Thus, in the following section, wind-tunnel experiments performed with symmetrical and asymmetrical arrangements of the energy harvester are explained.

4. Wind-Tunnel Tests

Energy harvesting from a flow is much more complex because of the fluid-structure interactions (FSI) taking place. Unlike in the case of the shaker, the flow input forcing function depends on the structure's geometry and mechanical properties (Connell & Yue, 2007). Previously, it was demonstrated that the offset configurations output higher levels of power compared to the case of bending only; here, we investigated whether this trend was the same in the case of the systems being immersed in a flow.

4.1 Experimental Setup

Experiments were carried out in an aeronautical wind tunnel. This wind tunnel is a closed circuit design having a test section measuring 1.07m in height, 1.32m in width and 2.7m in length. A six-bladed fan powered by a 100kW DC motor drives the airflow, and a 4:1 contraction ratio coupled with anti-turbulence meshes give longitudinal turbulence intensities of less than 0.3%. A pitot static tube connected to an MKS Baratron® was used to determine the flow speed.

Since the experiment involved recording of electrical output from the piezoelectric patches, a signal-to-noise ratio in the tunnel was evaluated. One end of a shielded coaxial cable was placed in the wind tunnel without touching the tunnel walls, and the other end connected to a 20MHz oscilloscope. The tunnel was set to a wind speed of 15.0m/s and the signal analysed. Then, the same wind speed was repeated, but with the actual piezoelectric element connected to the cable. The signal to noise ratio was found out to be about 350:1, so no

filters or corrections were required. The wind speed range chosen for the experiments was 3.0m/s to 8.0m/s. This range was chosen based on the average wind speeds in a representative urban area (Wind resources in Victoria, 2010). Experiments performed by Li and Lipson (2009) also investigated the same test range.

4.1.1 Configuration Setup

The PVDF patch used was identical to the one used in the shaker tests (Table 2). Three similar configurations were tested for their power output. An artificial "leaf" was fabricated from 0.35mm-thick polypropylene. The material had a density of 995kg/m^3 and an elastic modulus of 1.26GPa. The leaf used was an isosceles triangle with a base and height, each 80mm respectively. This geometry was chosen based on the work done in McCarthy et al. (2012).

In the symmetrical configuration, the PVDF patch was directly connected to the leaf via a revolute hinge as per Figure 8a. In the asymmetrical configurations, Mylar was used to create an offset between the axis of the leaf and the centroidal axis of the piezo (Figure 8b). The offset distances were kept the same as the ones used in shaker tests (i.e. *a* was 36 mm and *2a* was 72 mm.)

The leading edge of the PVDF patch was clamped using metal strips having a thickness of 1.75mm in all the three cases. The stand was guyed to the walls of the wind tunnel using thin-gauge wires, to avoid any transverse vibrations during the experiments. Previous flow visualization work indicated that the clamping strip and binder clips did not have any significant aerodynamic interference with the harvester (McCarthy et al., 2013).

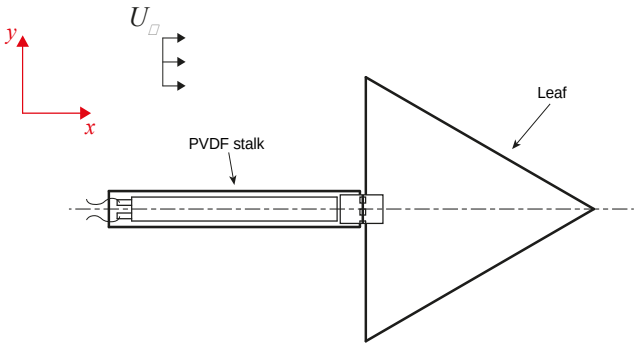

Figure 8a. Schematic diagram of pure bending (horizontal-stalk zero offset) configuration

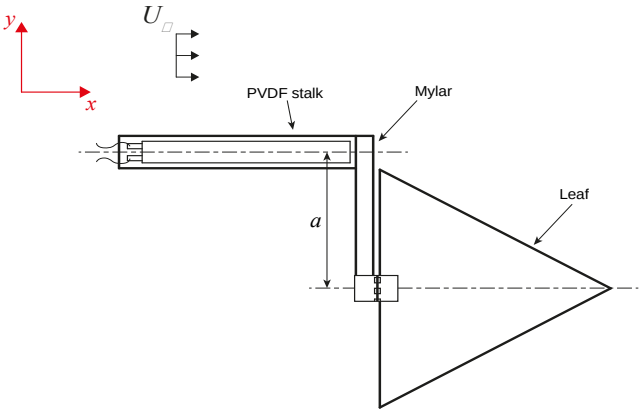

Figure 8b. Schematic of the asymmetric (*a*-offset) configuration

4.1.2 High Speed Image Capture

In order to highlight the flutter modes of the three configurations, high speed footage was captured for all the tested wind speeds. A high-speed camera (IDT X-Stream XS-4) was placed downstream of the specimen. An image of the setup is shown in Figure 9. The footage was acquired at 1000 frames/second to ensure good resolution of the leaf-stalk flutter and the specimen was lit with a 300W studio light from outside the wind tunnel. The electrical circuit and data acquisition methods were the same as in the dynamic tests.

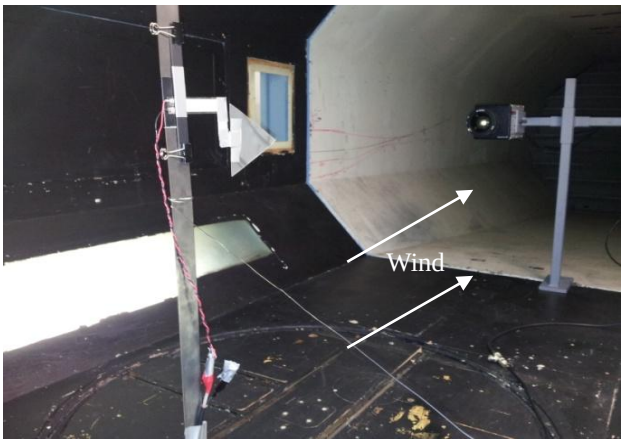

Figure 9. Asymmetrical configuration with camera setup in wind tunnel

4.2 Results and Discussion

4.2.1 Power Output

The output power was measured and recorded for two minutes for each wind speed, once flutter manifested for each configuration. The results for the mean power output at each wind speed with standard deviation for all the configurations are shown in Figure 10.

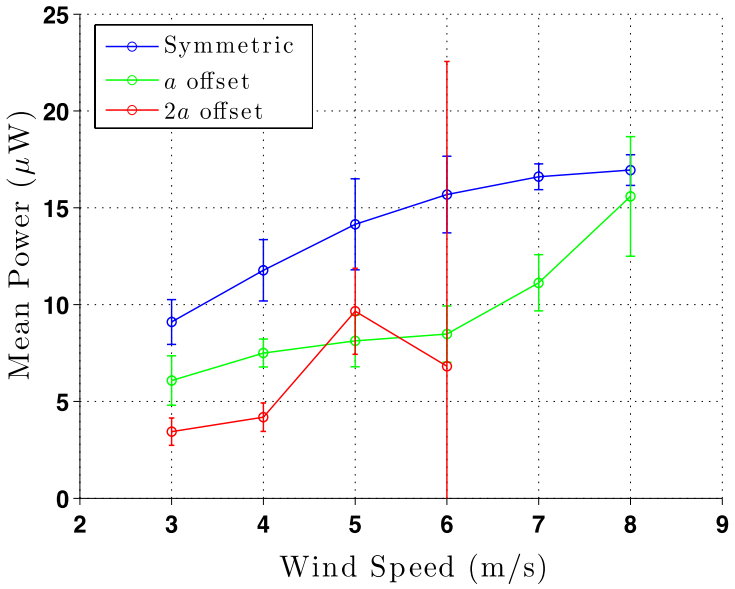

Figure 10. Power output of three piezo configurations versus wind speed

For the symmetric configuration, it was evident that as the wind speed increased, the power output also increased. This could be deduced visually from the experiments; as the wind speed increased, the flutter frequency of the PVDF patch also increased (Equations 11 and 12). Also, it was clear that the patch was subjected to only transverse bending due to the nature of fluid pressure impinging on leaf-stalk. A maximum power output of about 17 μW was observed at a wind speed of 8.0m/s. Flutter of this configuration consisted of limit-cycle oscillations with no random snap-through events occurring, similar to the flutter observed at higher flow speeds for a uniform filament in a parallel flow (Connell & Yue, 2007). This explains the relatively low output-power deviation at the higher wind speeds.

For the *a*-offset configuration, the power output increased as the wind speed increased but surprisingly, the power output remained lower than that of the symmetrical configuration for every wind speed. This was contrary to the dynamic test results, which suggested that the *a*-offset configuration would output more power due to

coupled bending-torsion vibrations. Furthermore, the *2a*-offset configuration showed no particular trend of the power output with monotonic increases in wind speed. The system had transitioned to flutter with large, non-linear deformations (explained in next section) and hence the system output power with high deviation in the case of the 5.0 and 6.0m/s wind speeds. At the higher wind speeds of 7.0m/s and 8.0m/s, the system interfered with the base clamp due to its chaotic flapping motion. Hence, the power output was not recorded at these wind speeds.

4.2.2 High-Speed Footage

High-speed imagery of the symmetrical configuration indicated that the PVDF was subjected to transverse bending at every wind speed. In the *a*-offset configuration, it was clearly seen that this configuration was subjected coupled bending-torsional modes. However, the amplitude remained lower than that of the pure bending configuration at every wind speed. In Figure 11, the point of maximum deflection for the symmetrical configuration is compared with that of the a-offset configuration at 6.0m/s. It can be seen from Figures 11a and 11b that the bending amplitude of the offset configuration was lower than that of the symmetrical configuration, meaning lower bending strain. However, it is also seen that the PVDF was subjected to some amount of torsional strain in the offset configuration.

In the asymmetrical cases, due to their geometry, the fluid forcing function impinging on the structure was no longer the same as the forcing function in the symmetrical configuration. In the dynamic tests performed earlier, the input forcing function was identical for all three cases. However, when the harvesters were immersed in a flow, there was a lack of direct control of the input fluid forcing function at a given wind speed, as it was totally driven by the structure's geometry (notwithstanding the flow properties being kept constant across all three test cases). However, comparing the flutter modes for each case provides some insight into the nature of the fluid forcing. Although the *a*-offset configuration experienced a small level of torsional strain, it was observed that the bending deflections were lower than the symmetrical configuration (Figure 11). As explained earlier, coupled bending-torsion vibrations involve bending and torsional strains. Although the *a*-offset configuration experienced torsional strain, the amount of bending strain would have remained lower compared to that of the symmetrical bending configuration. This was perhaps the cause for lower power outputs in the *a*-offset configuration.

It was interesting to observe the flutter pattern of the *2a*-offset configuration. Because the Mylar was longer, the system did not show evidence of limit-cycle oscillations, but rather manifested flutter in the chaotic regime, i.e. where irregular deformation magnitudes and random snap-through events occurred. The maximum deformation of the *2a*-offset configuration at 6m/s may be seen in Figure 12. The average power output recorded for this configuration was lower with a high standard deviation (Figure 10). At wind speeds of 7.0m/s and 8.0m/s, the flapping was very chaotic, to an extent that the leaf entangled itself with the base clamping strip and stalled. It has been shown elsewhere that maximum strain energy is acquired only when flutter eventuates in limit-cycle oscillations (Alben & Shelly, 2008). Thus, during chaotic flapping, the power output reduces drastically. The characteristics of different flutter regimes can also be found in Yamaguchi et al. (2000).

The two types of flutter, namely limit-cycle oscillatory and chaotic, may be distinguished visually from experiments; however, the existence of chaotic flutter may be more readily perceived by inspection of the output-voltage spectral density. Where limit-cycle oscillations over time produce a distinct peak at the flutter frequency, chaotic flutter characterizes a more broadband response, as can be seen in Figure 13. The flutter bending-mode harmonics are clearly seen in Figure 13a, whereas in Figure13b, a peak in the signal approximately one-half of the dominant limit-cycle frequency manifested; a common indication of transition to chaotic flutter (Connell & Yue 2007). Note that the dominant frequency in the bending case is higher and more pronounced than the *2a*-offset case, despite the constant wind speed, as noted by Argentina and Mahadevan, (2005), which partly lends to the greater output power of the bending case. Interestingly, the output-power deviation was almost identical between the bending and 2a-offset cases (Figure 10).

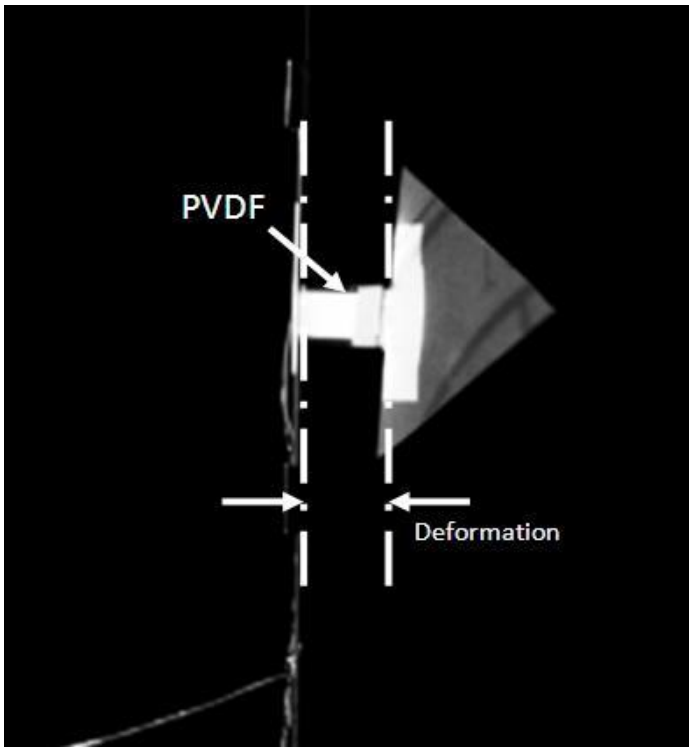

Figure 11a. Maximum deflection of the symmetrical case at 6.0m/s

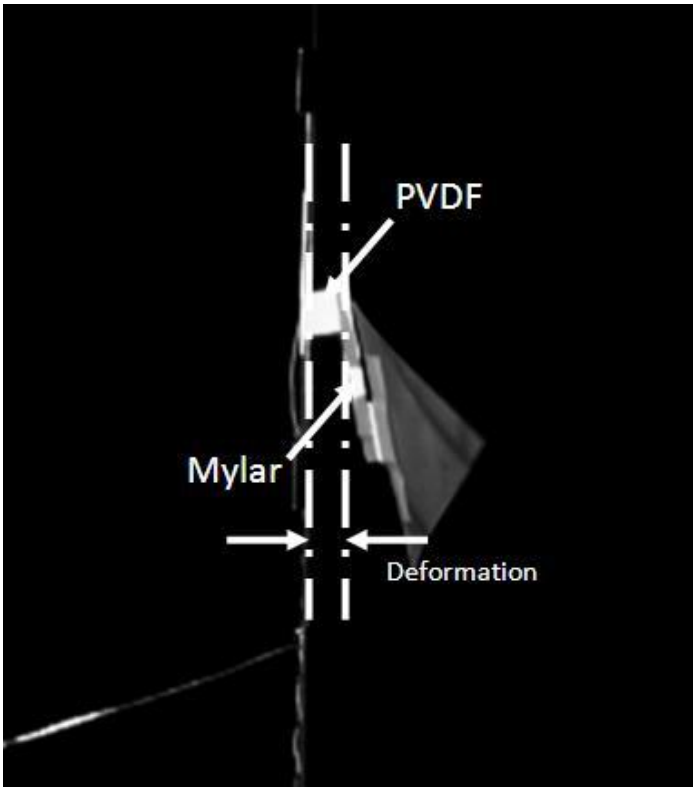

Figure 11b. Maximum deflection of the a-offset case at 6.0m/s

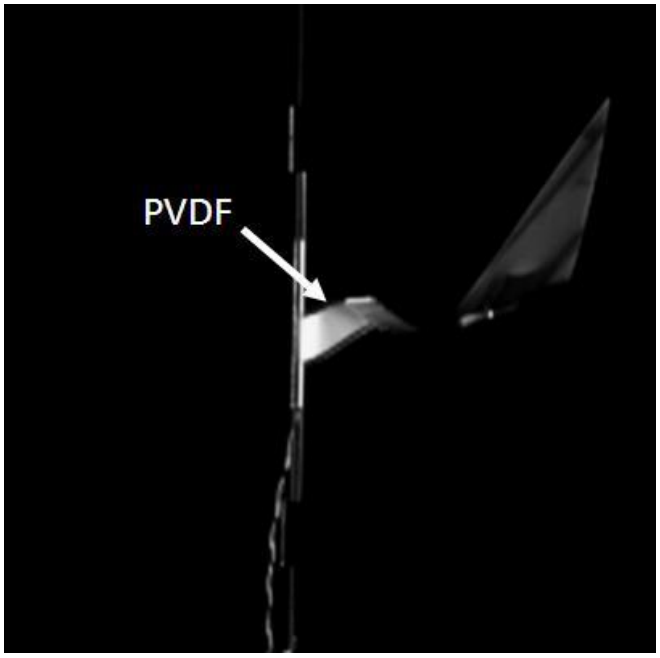

Figure 12. Maximum deformation of 2a-offset configuration at 6.0m/s

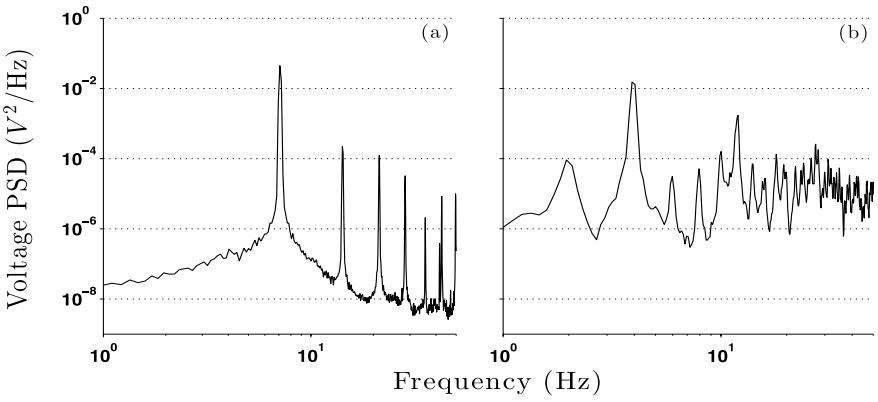

Figure 13. Voltage spectral density at 5.0m/s for the a) bending-only and b) *2a*-offset cases

In any piezoelectric material, the power output depends on its operational mode. Piezoelectric materials subjected to transverse bending operate in the d_{31} mode. However, when the material is subjected to torsion, in-plane shear strains and axial strains along the edges are experienced. Due to the poling, design and electrode configuration of the PVDF examined, the shear strains (the conventional d_{15} mode) do not contribute to the harvestable power. The bending strains induced by torsion alone contribute to the harvestable power. The induced strains along the width of the material operate primarily in d_{32} mode (Figure 14). In general, commercially available PVDF piezoelectric materials are not designed to work in the d_{32} mode and hence their corresponding strain coefficients are very low (Table 2). Thus, it is evident that although torsional vibrations induce combined strains, it cannot be a substitute for energy harvesting from transverse bending as only the bending strains induced by torsion contribute to the power output. It could only act as an additional source of power output. It is therefore essential to achieve more strain in d_{31} mode to obtain more power output. These asymmetrical configurations, although induced torsional vibrations, could not induce enough bending strains compared to the pure bending configuration. Also, the very low value of d_{32} conversion coefficient indicated that torsional vibrations do not help in providing more power output if enough amount of strain in d_{31} is not achieved. It is however important to note that the power output is proportional to the time rate of change of strains in any direction. Therefore, the comparison of the piezo coefficients only gives a fair understanding of the piezo's

behavior and does not provide any conclusive result.

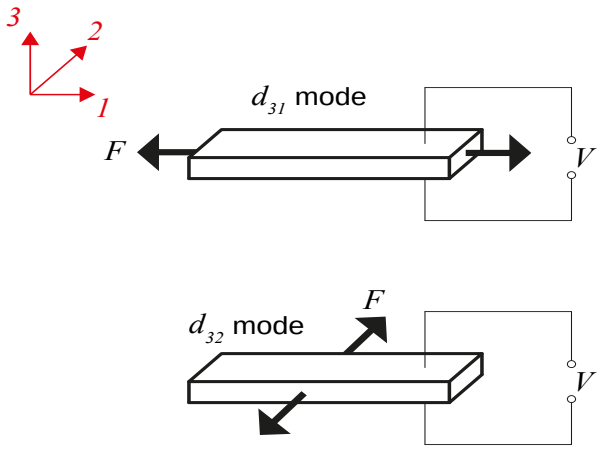

Figure 14. Piezo operational modes : d_{31}-bending; d_{32}-**torsion**

Another important drawback in these asymmetrical configurations is their low fatigue life. PVDF's subjected to excessive bending and torsional strain are prone to chaotic flapping and hence increased fatigue. During chaotic flapping, the PVDF is often subjected to high amounts bending and twisting, thereby causing high stress concentrations along the edges leading to reduced fatigue life. Also, since the power output was already lower compared to the pure bending case and more prone to chaotic flapping and fracture in a short amount of time, it would not be economically viable to design a harvester, with an asymmetrical configuration discussed here, to be excited by fluid flow, unless these PVDFs are specifically manufactured to work in bending-torsion modes of vibration.

4.3 Vertical-Stalk Configuration

In Li and Lipson (2009), a horizontal-stalk configuration was compared with the vertical-stalk configuration for its power output. It was mentioned that the vertical-stalk configuration provided much more power output compared to the horizontal configuration. However, the reason for the increased power output was not discussed in detail. In the following section, power output of the vertical-stalk configuration is compared with the horizontal-stalk configuration. High speed video results of the vertical-stalk configuration are also explained. Figure 15 shows the schematic of the vertical-stalk configuration where the axis of the PVDF is perpendicular to the direction of flow. The experimental, electrical and high speed camera setup were maintained the same as explained in the previous section.

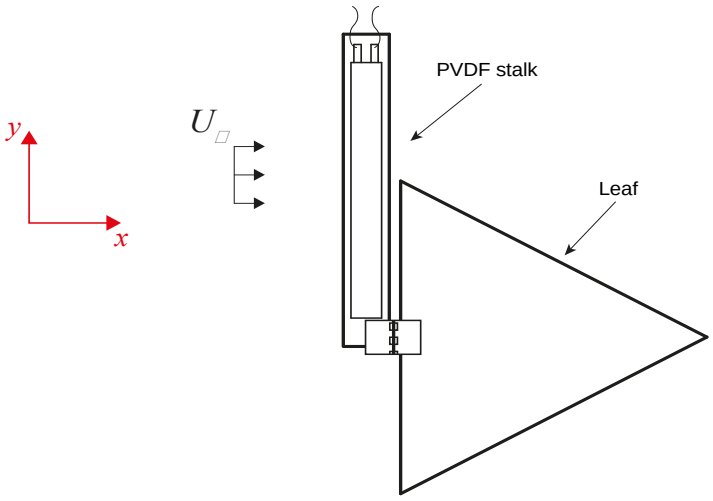

Figure 15. Schematic of vertical-stalk configuration.

4.4 Results

4.4.1 Power Output

The vertical-stalk experiments were performed in a similar manner to the horizontal-stalk experiments. The load resistance was maintained at 5.6MΩ throughout the experiment. The power outputs along with standard deviations of the vertical-stalk configuration are compared with horizontal-stalk pure bending configuration at different wind speeds are shown in Figure 16.

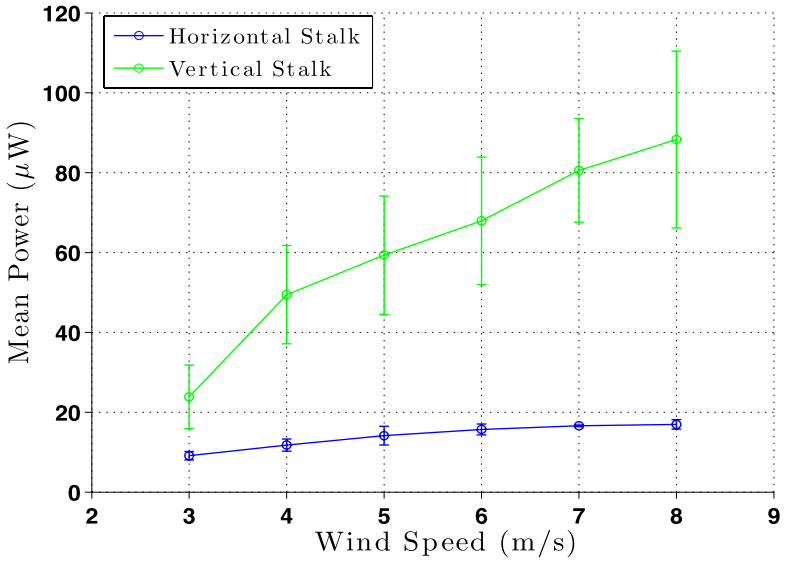

Figure 16. Power output vs. wind speed

The vertical-stalk configuration clearly provided more power output than the horizontal-stalk configuration, for all wind speeds tested. A maximum power of 88.3μW was observed at a wind speed of 8m/s from the vertical-stalk configurations. It is important to note that this power output could have been further increased by tuning the load resistance for this configuration at 8m/s, given its non-optimal load matching as mentioned above. From visual inspection, it was suspected that the PVDF stalk was subjected to excessive non-linear bending. However, due to the high flapping frequencies (8-25Hz), high speed capture of the leaf-stalk was required to confirm the hypothesis. Also, the standard deviations remained higher for the vertical-stalk configuration, indicating that the flutter pattern was less harmonic compared to the horizontal-stalk configuration. The cause for the excessive power output is explained with the help of high-speed video results in the next section.

4.4.2 High-Speed Footage

High-speed footage for the vertical stalk configuration was captured at 1000 frames/second. The camera was programmed to capture two seconds of footage. This was repeated for every wind speed, and the camera captured footage only few seconds after motion of the leaf-stalk occurred.

The maximum deformation of the PVDF stalk at a wind speed of 3.0m/s is shown in Figure 17. It is evident from this figure that the PVDF stalk was subjected to large transverse bending. This bending strain was augmented by a torsional strain at this point of maximum deformation. However, the amount of torsion induced in the stalk was considerably less compared to the bending. This behavior was also observed at other wind speeds. Thus, the increased power output in the vertical stalk configuration could be attributed to large non-linear bending deformations augmented by relatively small torsional deformations. In all the high speed footages, the wind has to be visualized as if flowing out of the images and the camera positioned as shown in Figure 9.

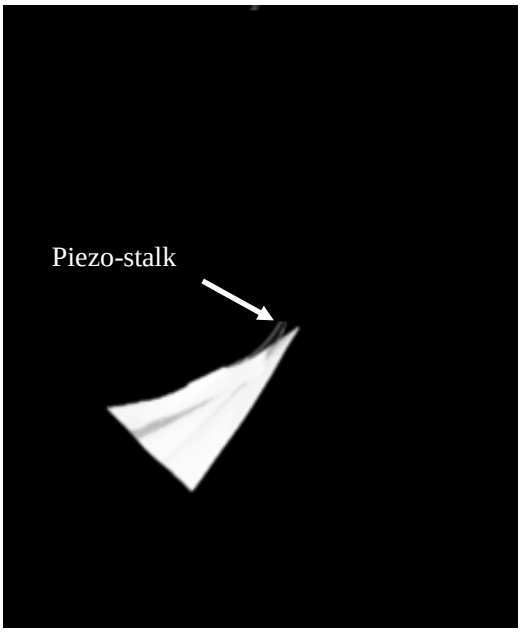

Figure 17. Maximum deformation of the PVDF stalk at 3.0m/s

The larger bending deformations in the vertical leaf-stalk arrangement were caused by the different nature of the aerodynamic forces impinging on the leaf, compared with the horizontal configuration. In the static-stable state (i.e. no flutter), the axis of rotation of the hinge was vertical with respect to the ground plane, for both configurations (Figure 1). However, the disparity in the aerodynamic forces arouse once the system began to flutter. In the vertical-stalk case, the hinge axis of rotation also tilted with the system. Figure 18 is an image of the flapper at 5.0m/s, where the hinge axis is virtually horizontal with respect to the ground plane. In contrast, the hinge always remained vertical with respect to the ground plane for the horizontal configuration during flutter. Given that the leaf-stalk flutter was mainly driven by the leaf, the leaf geometry did not change between the horizontal and vertical configurations, and the wind speeds tested were identical in both cases, it is proposed that unsteady lift forces were chiefly driving the vertical-stalk cycle. That said, it has not been quantitatively determined whether the magnitude of the lift forces were larger in the case of the vertical-stalk case. It can be argued that the changing direction and orientation of the lift forces did indeed act constructively out of phase with the structural deformations occurring in the piezoelectric stalk, with the vertical-stalk case. An in-depth investigation into the unsteady lift forces governing the motion of the vertical-stalk case was not included in the work here.

Due to the large structural deformations, the stalk-leaf system would strike the base clamping strips during every flutter cycle. This behavior was observed at wind speeds of 5.0m/s and higher. The piezo-leaf system would rotate almost 180 ° and impact the base clamping strips. The interference of the clamping strips on the motion of the flapper could have also been the cause for a marginal decrease in the gradient of the power curve after 4.0m/s (Figure 16). However, this issue was not resolved simply because the base of the stalk required secure clamping. An image of the flapper at 8.0m/s is shown in Figure 19, where the base clamp is seen to be interfering with the flutter motion of the piezo-leaf system.

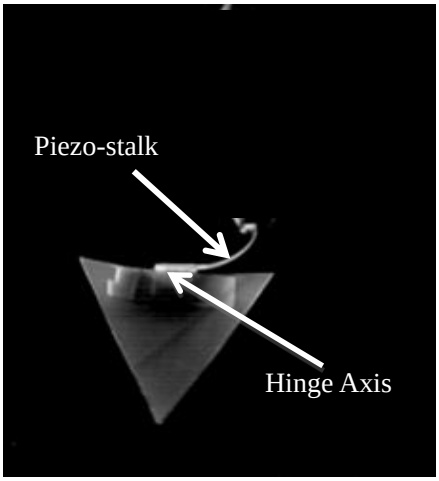

Figure 18. Entire surface of leaf facing the wind with an instantaneous horizontal hinge axis, at 5.0m/s

Figure 19. Image at 8.0m/s. Clamping strip interfering flapper motion

Figure 20. Crack observed at the clamping edge of the vertical stalk after 3 experimental trials

Although the large deformations result in increased power output, one major drawback is the fatigue life of the PVDF stalks. After the experimental trials, it was found that the piezoelectric patches cracked at the clamping location (Figure 20). This was probably due to the combination of excessively large bending displacements and fatigue. However, one way that this issue could be resolved is by increasing the stiffness of the stalk, by stacking the PVDF patches. The patches could be stacked with or without an air gap, which would reduce the large deformations prevalent using a single stalk. At the same time, relatively high power outputs could be obtained since the stalks could be electrically connected in parallel, thus the charge from each piezoelectric patch would be cumulative. It remains to be seen whether the lower deformations of a stacked configuration would trade off with the additional current provided in a stacked configuration. This would form a part of the future work in this configuration.

5. Conclusions

Energy harvesting from PVDF using coupled bending-torsion vibrations was investigated. Basic theoretical bending and torsion equations suggested that asymmetrical configurations would output more power compared to symmetrical configurations due to coupled bending-torsion strain. Dynamic tests were performed using a shaker to measure the power output for symmetrical and asymmetrical configurations and these results were computationally validated. It was clear that the offset configurations provided more power output compared to pure bending configurations. However, it was observed that the power generated could be significantly affected by the amount of structural damping present in the system.

Wind-tunnel tests were carried out for these configurations by coupling these configurations with an artificial leaf using a free hinge. It was somewhat surprising to find out that the offset configurations resulted in lower power outputs compared to the symmetrical pure bending configuration. However, high-speed video images indicated that amount of bending deformations induced in the offset configurations were lower. Due to the difference in geometry and flexibility of the configurations, the input fluid forcing function no longer was maintained constant. Thus, the amount of bending strain in the offset configurations remained lower. Also, the offset configurations, due to their flexibility, were more prone to chaotic flapping, thereby reducing the average power output. Most importantly, PVDFs subjected to coupled bending-torsion flutter partly operate in the d_{32} mode which has a relatively low piezoelectric conversion coefficient. Thus, the amount of power generated by the offset configurations remained low compared to the pure bending configuration at all wind speeds.

It was observed that the vertical-stalk configuration provided much more power output compared to the symmetrical horizontal-stalk configuration. High speed videos indicated that this was because of excessive non-linear bending strain augmented by small amounts of torsional strain experienced by the PVDF. However, it was observed that these PVDF films were prone to fatigue and fracture due to the large amounts of strain. Thus, it was understood that harvesters subjected to coupled bending and torsion modes of flutter were more prone to chaotic type of flapping and fatigue, hence they produced lower amounts of power. This also indicated that it is not economically viable to design a harvester, subjected to bending-torsion modes of flutter, unless the piezoelectric materials are specially designed to withstand high bending and torsional strains. Also, due to the current design of most commercially available PVDFs which operate primarily in d_{31} or d_{33} modes, it is understood that energy harvested in fluid flow from torsion could only act as a low-value peripheral supplement to the energy harvested from bending.

Acknowledgments

This work was funded under Australian Research Council (ARC) Linkage grant LP100200034 in conjunction with the Partner Organisation - Fabrics & Composites Science & Technology (FCST) Pty Ltd.

References

Abdelkefil, A., Najar1, F., Nayfeh, A. H., & Ben A. S. (2011). An energy harvester using piezoelectric cantilever beams undergoing coupled bending–torsion vibrations. *Journal of Smart Materials and Structures, 20*, 115007 (11pp). http://dx.doi.org/10.1088/0964-1726/20/11/115007

Alben, S., & Shelly, M. J. (2008). Flapping states of a flag in an inviscid fluid: Bistability and transiton to chaos. *Physical review letters, 100*, 074301. http://dx.doi.org/10.1103/PhysRevLett.100.074301

Allen, J. J., & Smits, A. J. (2001). Energy harvesting eel. *Journal of Fluids and Structures, 15*(3-4), 629–640. http://dx.doi.org/10.1006/jfls.2000.0355

Argentina, M., & Mahadevan, L. (2005), Fluid-flow-induced flutter of a flag. *Proceedings of the National Academy of Sciences of the United States of America, 102*(6), 1829–1834. http://dx.doi.org/10.1073/pnas.0408383102

Beards C. F. (1996). *Structural Damping: Analysis and Damping*. Elsevier, ISBN: 978-0-340-64580-2.

Bryant, M., Mahtani, R., & Garcia E. (2011). Synergistic wake interactions in aeroelastic flutter vibration energy harvester arrays. In *ASME Conference on Smart Materials, Adaptive Structures and Intelligent Systems, SMASIS*, September 18 - September 21, American Society of Mechanical Engineers.

Connell, B. S. H., & Yue, D. K. P. (2007). Flapping dynamics of a flag in a uniform flow. *Journal of fluid mechanics, 581*, 33-67. http://dx.doi.org/10.1017/S0022112007005307

Datta, S. K., & Gottenberg, W. G. (1975). Instability of an elastic strip hanging in an airstream. *Journal of Applied Mechanics, 42*, 195–198. http://dx.doi.org/10.1115/1.3423515

Deivasigamani, A., McCarthy, J. M., John, S. J., Watkins, S., & Coman, F. (2013). Flutter of cantilevered interconnected beams with variable hinge positions. *Journal of fluids and structures, 38*, 223-237. http://dx.doi.org/10.1016/j.jfluidstructs.2012.10.011

Dickson, R. (2008). New Concepts in Renewable Energy. Lulu Enterprises, Inc.

Erturk, A., & Inman, D. J. (2011). *Piezoelectric energy harvesting*. John Wiley and Sons, Ltd., ISBN: 978-0-470-68254-8. http://dx.doi.org/10.1002/9781119991151

Kong, N., Ha, D.S., Erturk, A., & Inman, D. J. (2010). Resistive impedance matching circuit for piezoelectric energy harvesting. *Journal of Intelligent Materials Systems and Structures (JIMSS), 21*, 1293. http://dx.doi.org/10.1177/1045389X09357971

Li, S., & Lipson, H. (2009). *Vertical-stalk flapping-leaf generator for wind energy harvesting.* In ASME Conference on Smart Materials, Adaptive Structures and Intelligent Systems, SMASIS, September 21-September 23, Vol. 2, American Society of Mechanical Engineers, pp. 611–619.

Li, S., Yuan, J., & Lipson, H. (2011). Ambient wind energy harvesting using cross flow fluttering. *Journal of Applied Physics, 109*(2). http://dx.doi.org/10.1063/1.3525045

Lord Rayleigh. (1879). On the instability of jets. *Proc. of London Mathematical Society, 9*, 4-13.

McCarthy, J. M., Deivasigamani, A., John, S. J., Watkins, S., & Coman, F. (2012). The Effect Of The Configuration Of The Amplification Device On The Power Output Of A Piezoelectric Strip. *ASME conference Smart Materials, Adaptive Structures and Intelligent Systems (SMASIS)*, Georgia, United States, SMASIS2012-7951.

McCarthy, J. M., Deivasigamani, A., John, S. J., Watkins, S., & Coman, F. (2013). Downstream flow structures of a fluttering piezoelectric energy harvester. *Journal of Experimental Thermal and Fluid Sciences* (in press). http://dx.doi.org/10.1016/j.expthermflusci.2013.08.010

Païdoussis, M. (1998). *Fluid-Structure Interactions - Slender Structures and Axial Flow*, 1. Elsevier Academic Press.

Pobering, S., & Schwesinger, N. (2004). *A novel hydropower harvesting device.* In International Conference on MEMS, NANO and Smart Systems, ICMENS, August 25 - August 27, IEEE Computer Society, pp. 480–485.

Priya, S. (2007). Advances in energy harvesting using low profile piezoelectric transducers. *Journal of electroceramics, 19*, 165-182. http://dx.doi.org/10.1007/s10832-007-9043-4

Sodano, H. A., Park, G., & Inman D. J. (2001). Estimation of electric charge output for piezoelectric energy harvesting. *Strain, 40*, 49-58. http://dx.doi.org/10.1111/j.1475-1305.2004.00120.x

Theodorsen, T. (1949). General theory of aerodynamic instability and the mechanism of flutter. *National Advisory Committee for Aeronautics*, Technical Report No. 496.

Timoshenko, S. (1963). *Strength of materials*. McGraw Hill Ltd., New York.

Weaver Jr. W., Timoshenko, S. P., & Young, D. H. (1990). *Vibration problems in engineering* (5th ed.). John Wiley and Sons, Ltd.

Wind Resources in Victoria. (2010). *Sustainability Victoria*. Retrieved December 26, 2011, from http://www.sustainability.vic.gov.au/www/html/2111-wind.asp%3E

Yamaguchi, N., Sekiguchi, T., Yokota, K., & Tsujimoto, Y. (2000). Flutter limits and behaviors of a flexible thin sheet in high-speed flow–II: Experimental results and predicted behaviors for low mass ratios. *ASME Journal of Fluids Engineering, 122*, 74–83. http://dx.doi.org/10.1115/1.483228